Journal of Colloid and Interface Science 630 (2023) 666–675

Contents lists available at ScienceDirect

Journal of Colloid and Interface Science

journal homepage: www.elsevier.com/locate/jcis

In-situ and quantitative imaging of evaporation-induced stratification in binary suspensions

Ellard Hooiveld [a], Hanne M. van der Kooij [a], Marijn Kisters [a], Thomas E. Kodger [a], Joris Sprakel [b], Jasper van der Gucht [a,*]

[a] Physical Chemistry and Soft Matter, Wageningen University & Research, Stippeneng 4, Wageningen 6708 WE, the Netherlands
[b] Laboratory of Biochemistry, Wageningen University & Research, Stippeneng 4, Wageningen 6708 WE, the Netherlands

GRAPHICAL ABSTRACT

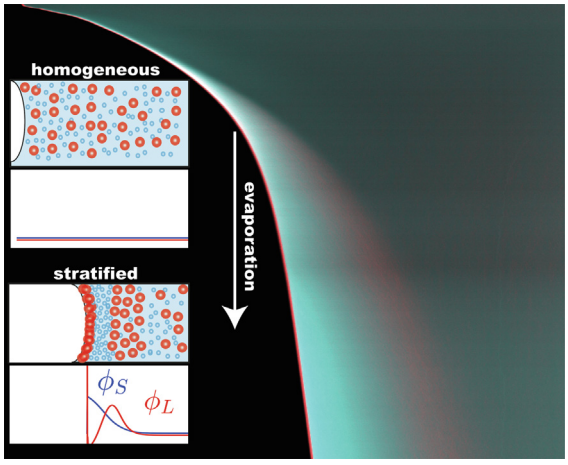

ARTICLE INFO

Article history:
Received 1 August 2022
Revised 5 October 2022
Accepted 20 October 2022
Available online 27 October 2022

Keywords:
Coating
Colloidal dynamics
Binary Suspension
Evaporation
In-situ Fluorescence Imaging
Stratification
Jamming
Diffusiophoresis
Non-equilibrium thermodynamics

ABSTRACT

The drying of a multi-component dispersion, such as water-based paint, ink and sunscreen to form a solid film, is a widespread process. Binary colloidal suspensions have proven capable of spontaneous layer formation through size segregation during drying. To design bespoke stratification patterns, a deeper understanding of how these emerge is crucial. Here, we visualize and quantify the spatiotemporally evolving concentration profiles *in situ* and with high resolution using confocal fluorescence microscopy of custom-designed binary dispersions in a well-defined geometry. Our results conclusively establish two distinct stratification routes, which give rise to three layered structures. A first thin layer develops directly underneath the evaporation front in which large particles are kinetically trapped. At later times, asymmetrical particle interactions lead to the formation of two subsequent layers enriched in small and large particles, respectively. The spatial extent and magnitude of demixing strongly depend on the initial volume fraction. We explain and reproduce the experimental concentration profiles using a theoretical model based on dynamic arrest and higher-order thermodynamic and hydrodynamic interactions. These insights unravel the key mechanisms underlying colloidal auto-stratification in multi-component suspensions, and allow preprogramming of stratification patterns in single-deposition formulations for future applications.

* Corresponding author.
E-mail address: jasper.vandergucht@wur.nl (J. van der Gucht).

https://doi.org/10.1016/j.jcis.2022.10.103
0021-9797/

1. Introduction

Drying of multi-component colloidal dispersions is an everyday phenomenon occurring in paints, coatings, cosmetics, adhesives, inks, mud puddles and many more materials[1–5]. Yet, at the microscale, this evaporation process is far from mundane, featuring an intricate interplay of hydrodynamics, mechanics, colloidal stability, and manifold interactions. These phenomena evolve heterogeneously in time and space, to ultimately determine the spatial architecture of the dry colloidal packing[6]. In this structure, colloids of different sizes can be autonomously separated in distinct layers. Leveraging auto-stratification to confer depth-dependent functionalities is a promising alternative to the current approach of sequential depositions, which is laborious, time-inefficient and costly.

Auto-stratification can occur via different pathways: (i) sedimentation or creaming, in which gravity acts upon particles with density larger or smaller than the medium, respectively. Heavy particles will be inclined to sink to the bottom, whereas light particles will tend to float upwards[7,8]. (ii) Marangoni flows arising from gradients in interfacial tension may lead to differential particle fractionation in drying droplets[9]. (iii) Particle adsorption at the liquid–air interface can create a monolayer of a specific type of particles at the top of the film[10]. (iv) A recently described pathway relies on the interplay between particle species of distinct sizes, mediated by asymmetric interactions, to achieve stratification[11]. In this work we focus on harnessing and understanding the latter segregation process.

To describe this segregation process, we start with the well-established drying of a monodisperse particle dispersion[12]. In the absence of sedimentation, two competing phenomena can be discriminated, namely (i) particle diffusion, and (ii) motion induced by the descending evaporation front. The competition between these two factors is captured in the dimensionless Péclet number, $Pe = \frac{Hv}{D}$[6,12,7,11], with H the initial film thickness, v the evaporation speed of the descending interface, and D the particle diffusion constant. When $Pe \gg 1$, particles become trapped at the interface, because their diffusion cannot keep up with the receding interface. By contrast, $Pe \ll 1$ implies that particle diffusion outpaces the solvent evaporation, causing the particles to remain randomly distributed throughout the film during drying.

A key parameter influencing the particle distribution is the diffusion coefficient, which for dilute spherical colloids is given by the Stokes–Einstein relation: $D = \frac{k_B T}{6\pi\eta R}$, with k_B the Boltzmann constant, T the temperature, η the viscosity of the solvent, and R the hydrodynamic radius of the particle. Different Péclet numbers can therefore be introduced by differently sized particles in one dispersion, for example a binary dispersion featuring a small (Pe_S) and large (Pe_L) Péclet number[12,6]. According to diffusion theory and experimental evidence, if $Pe_S \ll 1$ and $Pe_L \gg 1$, the large particles will accumulate at the top, thus depleting the small particles and giving rise to 'large-on-top' stratification[12,13]. However, the situation changes when both Pe_S and $Pe_L \gg 1$, for which the counter-intuitive 'small-on-top' stratification has been found in both experiments and simulations[11,7]. In this scenario, small and large particles are jointly trapped at the evaporation interface, creating concentration gradients and associated osmotic pressure gradients perpendicular to the evaporation front. These gradients drive both types of particles away from the interface through diffusion and diffusiophoresis, which is the migration of one particle species due to the concentration gradient of the other species [14,7,15,16]. Combining the diffusiophoretic force with the primary counter force, i.e. viscous drag, results in a higher velocity of the large particles away from the evaporation front compared to the small particles, ultimately leading to a small-on-top stratified dry film[7,11].

Diffusiophoretic size segregation is governed by thermodynamic interparticle forces. These interactions were first modeled via a hard-sphere approximation and second-order virial expansion of the free energy[17], and recently extended to more complex potentials[16]. For dilute dispersions, these theories are consistent with experimental data, but for higher ϕ_S (>0.10) they fail to provide correct predictions[7]. Also with implicit solvent simulations, i.e. Langevin and Brownian Dynamics[18,19,11,5,20,13], the stratification could be reasonably predicted. However, by switching from implicit to explicit solvent models, a much smaller parameter window for small-on-top stratification was found[21,22]. Clearly, hydrodynamic interactions cannot be neglected. In addition to osmotic pressure gradients stemming from particle accumulation, also solvent pressure gradients arise, which lead to solvent backflow that counteracts the colloidal fractionation[15,14]. Yet, experimental techniques have failed to measure how all these forces dynamically interact, and how they lead to the final stratified film.

Experimental methods to study stratified coatings *a posteriori* are atomic force microscopy and scanning electron microscopy (SEM), which elucidate the particle size distribution at the top of the film only, while cross-sectional SEM, Raman spectroscopy, energy-dispersive X-ray spectroscopy, elastic recoil detection, confocal microscopy, and small-angle X-ray scattering (SAXS) have been used to reveal the depth distribution of different particles[11,18,12,23–25,5,2,26–33]. These methods have identified key parameters influencing the extent of demixing, notably the size ratio of the two particle types[32,17,15,31], particle polydispersities[19], initial particle concentrations[11,15], particle interactions[12], evaporation rate[24,11], and medium viscosity[34]. For a comprehensive overview of the respective effects, we refer to a recent review by Schulz and Keddie[7]. Although previous studies have yielded valuable insights into how to tune the stratification pattern of the final dried film, they fail to show the layer development and the influence of all these parameters during evaporation. To obtain a quantitative understanding of the stratification process, a method is therefore needed that makes it possible to follow the evolution of the concentration profiles in real time.

To measure the temporal evolution of size segregation, drying states at specific time points can be fixated by rapid freezing. Cryo-SEM subsequently allows unveiling the particle distribution of freeze-fractured cross-sections[35,36]. However, this procedure is laborious, prone to artefacts, and lacks access to particle dynamics. Recently, SAXS proved to be an alternative candidate, but the inherent analysis in reciprocal space makes it challenging to extract meaningful and intuitive quantities[37].

In this paper, we use confocal fluorescence microscopy to visualize stratification in a drying binary colloidal dispersion in real time. While this method has been successfully applied to resolve particle concentration profiles[38–40] its potential to shed more light on the stratification mechanism is still untapped. By precisely matching the density and refractive index of fluorescent particles to the solvent, we are able to quantify the spatiotemporally developing concentration gradients of both particle populations with high resolution. A well-defined capillary geometry allows us to mimic unidirectional film drying in a controlled manner. Furthermore, we present a theoretical model that incorporates higher-order particle–particle interactions, solvent backflow, and the formation of a jammed layer, to fully describe the particle segregation process. This unique combination of experiments and theory enables us to unravel the mechanisms underlying auto-stratification in drying multi-componentdispersions with a high level of accuracy.

2. Materials and methods

2.1. Particle synthesis

The materials used in this study and elaborate synthesis protocols are provided in **SI 1.1–1.5**. In brief: small particles (0.46 ± 0.04 μm, **Fig. S1**) and large particles (1.6 ± 0.06 μm, **Fig. S1**) were synthesized by surfactant-free emulsion polymerization and dispersion polymerization, respectively[41,39]. The small particles were fluorescently labeled by adding the dye (pyrromethene 546) to the monomer phase. The large particles were fluorescently labeled by trapping the dye (pyrromethene 650) after swelling. Both particle species were almost perfectly refractive index and density-matched with the solvent formamide by using a 24:76 ratio (v/v) of the monomers tert-butyl methacrylate and 2,2,2-trifluoroethyl methacrylate. See **SI 1.6** for details about the particle characterizations.

2.2. Preparation of evaporation chambers

Capillaries (Vitrocom nr. 5012–050, 10 mm in length) were glued to microscope slides (1 mm thickness) with Norland optical adhesive 61 (NOA 61), whose refractive index is similar to that of glass after curing, here achieved by illumination with UV light for ~10 min (366 nm, Camag UV lamp 4). The surfaces of the capillaries were modified in two steps: first, they were activated using a plasma cleaner (Anadis instruments) for ~2 min. Thereafter, they were reacted with a mixture of 425 μl 3-chloropropyltrimethoxysilane and 75 μl trichloro(1H,1H,2H,2H-perfluorooctyl) silane in a glass vial for ~3 h at 70 °C in a vacuum atmosphere (desiccator) via vapor deposition. This ratio was empirically found to optimize the contact angle with formamide to slightly below 90°, such that the particles did not stick to the glass (which causes additional solvent flows, see **Fig. S2**), yet the dispersion would still enter the capillaries through capillary suction. The surface-modified capillaries were subsequently filled with ~1 μl sample with different initial volume fractions of small and large particles. Their ends were sealed with NOA 61 that was partly taken up in the capillary, and cured with a 365 nm UV LED (OmniCure LX 300, 320 mW). This ensured that the sample would dry only at one side of the capillary, thus providing a 1D evaporation profile. The reference samples for a calibration to determine the volume fractions from the fluorescent intensities were created in the same manner, yet with both ends closed using NOA 61.

2.3. Controlled drying and fluorescence imaging

The fluorescence signal of both dyes was collected in the horizontal direction. Evaporation was initiated and maintained by applying a low pressure (100 mbar, 22 ± 1°C) to the filled capillaries using a pressure adjustable vacuum pump in a custom-made 3D printed vacuum chamber, that fitted precisely inside the microscope stage (**Fig. S3**). This chamber was closed by pressing the microscope slides onto a polydimethylsiloxane (PDMS) rubber slab (glued to the vacuum chamber), so that the chamber became airtight. The drying of the sample and the concentration of both particle populations were followed using an inverted Nikon C2 confocal laser scanning microscope and a 4× air objective (NA 0.15) to capture a large part of the capillaries around the evaporation front. The fluorescent dye of the small particles was excited at 488 nm, and fluorescence was collected between 500 and 525 nm. The fluorescent dye of the large particles was excited separately at 564 nm, and the emission was collected between 575 and 615 nm. In this way the fluorescence signals of the two particles were well separated, and no significant cross-talk between the dyes was found. The fluorescence images were collected every minute over a time span of ~22 h. Note that in this time span, complete evaporation of the sample was not reached. Further details about the data analysis can be found in **SI 1.7**.

3. Results and discussion

3.1. Experimental set-up

To measure evaporation-induced stratification in time, we insert a binary colloidal dispersion into a well-defined capillary (**Fig. 1**). We close one side to impose one-dimensional drying from the open end, thus resembling top-down evaporation of typical coatings. The dispersion consists of two types of custom-synthesized polymer colloids: small particles with a diameter of 0.46 ± 0.04 μm and large particles of with a diameter of 1.6 ± 0.06 μm (**Fig. 1b**, **Fig. S1**). By using a specific ratio of two co-monomers, the particles have a refractive index and density that matches the dispersing fluid formamide[39]. Onto the surfaces of the particles, a slightly negatively charged polymer brush is covalently attached, to provide steric and electrostatic stabilization and identical particle surfaces. The two types of particles are each labelled with a fluorescent dye, which are spectrally separated.

We start our experiments with initial volume fractions of 0.050 and 0.025 for the small ($\phi_{S,0}$) and large ($\phi_{L,0}$) particles, respectively. The capillary is positioned in a pressure-controlled atmosphere, which we reduce to 100 mbar (**Fig. S3**). This set-up yields highly similar evaporation rate profiles for the different experiments (**Fig. S4**). At the onset of drying, both particle species are homogeneously distributed throughout the capillary. However, near the evaporation front a narrow zone of predominantly large particles is visible immediately after the reduction of the pressure (**Fig. 1c**). After approximately 20 h, a clear change in fluorescence intensities starts to occur: small particles accumulate directly behind the intense band at the front, while large particles accumulate further away from the evaporation front.

3.2. In-situ imaging of stratification

During the first ~4 h, both small and mainly large particles accumulate at the evaporation front, which essentially sweeps up the colloids (**Fig. 2**). Since the particles cannot diffuse away sufficiently fast to homogenize the concentration throughout the capillary, a sharp inhomogeneity in fluorescent intensity near the evaporation front arises rapidly at the start, when the drying rate is highest (**Fig. S4b**). This layer remains intact, and the constituent particles remain immobilized during the following evaporation stages (**Fig. 2**, **Movie S1**). Most likely, the strong and long-ranged electrostatic interactions between the charged particles [42] in this layer lead to a liquid-to-solid transition, so that a dynamically arrested layer is formed at the evaporation interface[43]. This jammed layer contains a pronounced excess of large particles. We note that this excess of large particles near the front is not the result of preferential adsorption at the air/liquid interface. However, while the large particles do not adsorb significantly, the small particles do form an adsorbed monolayer at the interface (**Fig. S10**). This layer of small particles is not visible at the resolution used in **Fig. 2**, but becomes apparent at higher magnification (**Fig. S10**).

As time progresses, the evaporation front propagates further inwards, thus lengthening the path that the solvent vapor molecules need to travel through the capillary. As a result, the evaporation rate decreases and the Péclet number is reduced proportionately (**Fig. S4b**). After ~4 h, the jammed layer does not

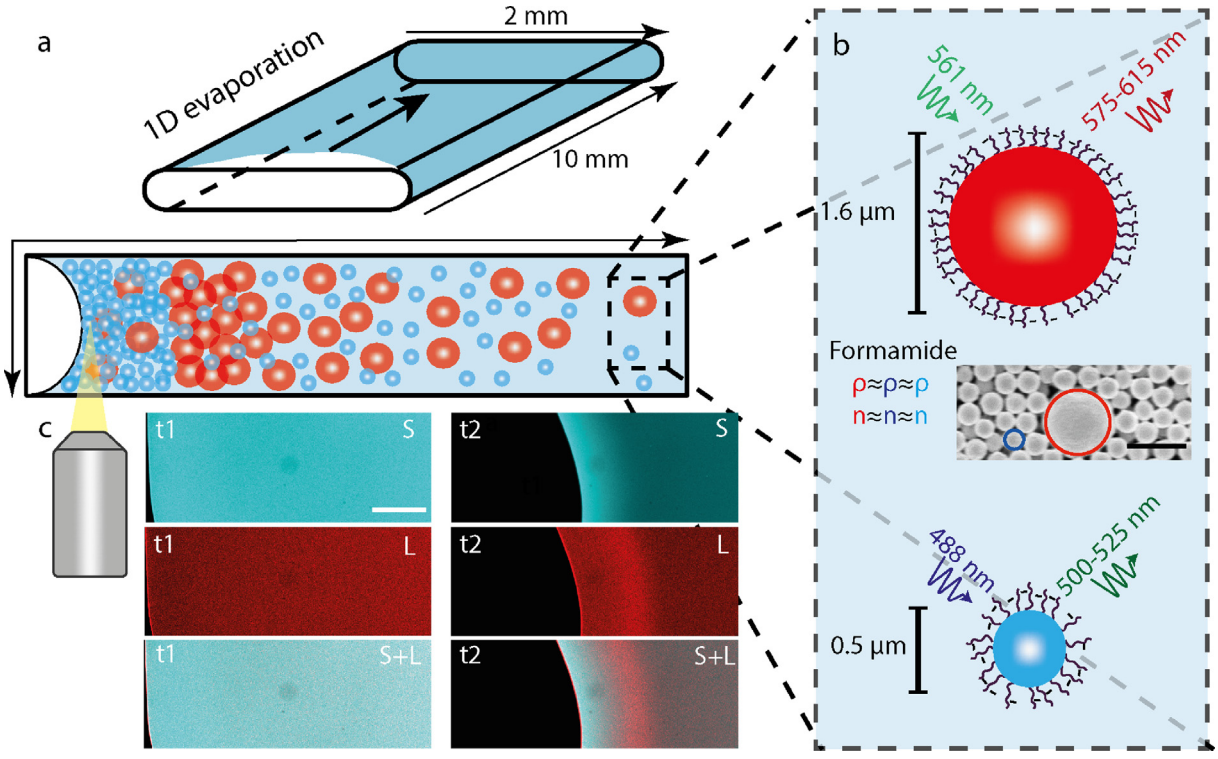

Fig. 1. In-situ imaging of evaporation-induced stratification in a binary suspension. a) Schematic of the capillary used to mimic and control 1D evaporation. At the back the capillary is closed, ensuring inward solvent flow.b) Magnification of the colloids, which are labeled with dyes providing good separation of emission wavelengths, as indicated. The particles feature identical polymer brushes at the surface, and are density- and refractive-index matching with the solvent. In the scanning electron micrograph, the two particles are delineated. The scale bar represents 1.0 μm. c) Representative fluorescence measurements in the early stages (t_1,after $\sim$ 0 h) and later stages (t_2,after $\sim$ 20 h) of drying. The top row shows the small particle signal, the middle row the large particle signal, and the bottom row the overlay. The scale bar represents 0.25 mm for all confocal images. With this experimental set-up we are able to follow the changing fluorescence intensities of both particle species during drying.

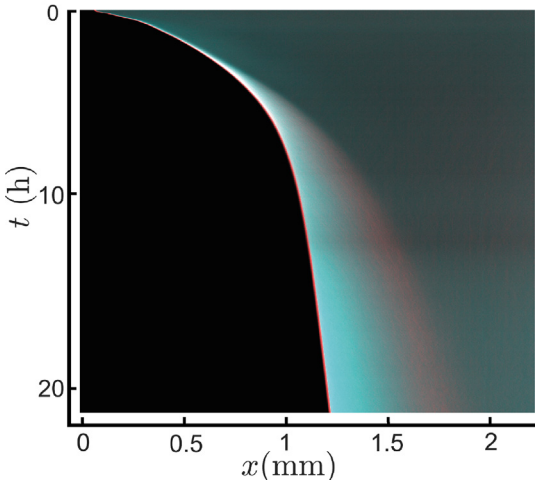

Fig. 2. Superimposed kymograph of the average fluorescence intensity of 10 pixel rows in the middle of the capillary of a drying suspension with $\phi_{S,0}$=0.050 and $\phi_{L,0}$=0.025. The increasing black region at the left indicates the drying of the sample. From the start a red band is visible indicating an excess of large particles in the jamming layer. From t$\sim$4 h the evaporation rate decreases, and concentration gradients start to occur deeper in the sample.

grow thicker anymore, but instead the accumulating particles retain their mobility and give rise to more gradual concentration gradients behind the jammed layer (**Fig. 2**). In line with well-established theories, osmotic pressure gradients consequently develop, which lead to particle self-diffusion and collective diffusion away from the evaporation front[44–46]. In addition, the two particle species segregate due to diffusiophoresis, which disproportionately affects the large particles: the net force exerted on them by small particles is much greater than the other way round[14,7,15]. This asymmetry leads to an excess of small particles directly behind the jammed region, while the large particles are expelled from this layer into a band with higher concentration further away from the evaporation interface (**Fig. 2**). Continued evaporation ultimately leads to an enrichment of small particles behind the jammed layer and of large particles near the closed end of the capillary. See **Movie S1** for the full time series of all the collected images.

Note that exclusively probing the air interface of this sample would reveal a predominance of large particles. In some earlier research, this was erroneously considered the only form of stratification, as deeper layers remained obscured. Our findings thus open the way for re-evaluation of existing literature in which only the end state is analyzed. In reality, the evaporating binary colloidal dispersion can be subdivided into different regions: (I) directly at the evaporation front a jammed, solid-like phase is formed, because the particles cannot escape this boundary sufficiently fast and thus get trapped in a jammed zone where diffusion is severely halted; (II) tens of μm away from the interface, a relatively concentrated phase of mobile particles develops, from which large particles are expelled by the small particles due to diffusiophoresis; (III) around $x \approx 0.5$ mm the expelled large particles gather, and (IV) a final region corresponding to the homogeneous bulk of the sample, which gets progressively depleted.

To obtain insight into the developing concentration profiles of both particle species (**Fig. 3a**), we convert these confocal micrographs into 1D fluorescence intensity profiles of both channels, while accounting for the curvature of the evaporation front

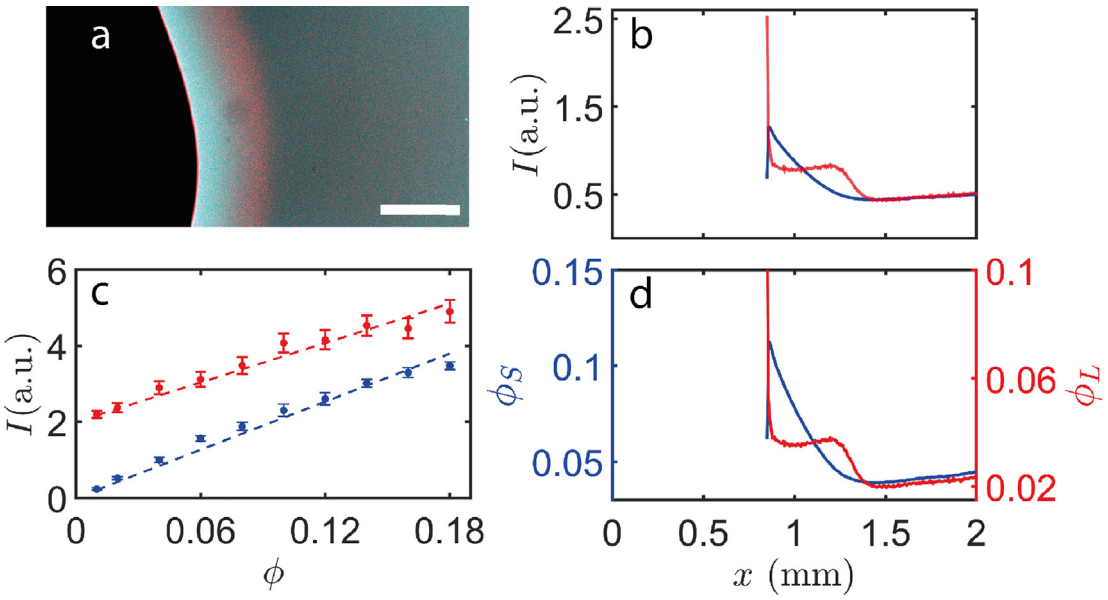

Fig. 3. a) Representative confocal micrograph with superimposed large (red) particle fluorescence and small (blue) particle fluorescence after 13 h of evaporation. b) Average fluorescence intensities of the small and large particles in blue and red, respectively, computed by averaging all pixels with a certain distance to the evaporation front in (a). c) Fluorescence intensity versus ϕ_S and ϕ_L, offset by 2 for the large particles for clarity. The solid lines are linear fits to the data. The error bars represent the standard deviations over all intensities of the pixels in one image of the homogeneous samples. d) Linear conversion of the fluorescence signals in (b) to ϕ_S and ϕ_L, using the fit results in (c). This routine allows quantifying 1D concentration profiles of both particle species for every confocal micrograph.

(Fig. S5), and plot these intensities I against the distance to the initial position of the evaporation front (x) (Fig. 3**b**). Since the fluorescence intensities are linearly related to the volume fraction of the small (ϕ_S) and the large (ϕ_L) particles within our range of interest, as validated from concentration series (Fig. 3**c**), we can directly convert the fluorescence intensities to 1D volume fraction profiles of the two particle populations (Fig. 3**d**). This method enables us to independently measure both ϕ_S and ϕ_L throughout the capillary during drying.

3.3. Effects of the initial volume fraction

An important tuning knob for the segregation of the particles is $\phi_{S,0}$, as predicted by different theoretical models and experimentally witnessed in the final dry state[17,16,24,29,7]. However, no experimental work addresses how this influences the temporal evolution, which is essential to fathom the underlying mechanisms. This temporal evolution of the concentration profiles can be obtained following the procedure described above. To investigate how $\phi_{S,0}$ affects the evolution of the concentration profiles in the different regions, we change $\phi_{S,0}$ to 0.025 and 0.10, while keeping $\phi_{L,0}$ constant. For all samples, a sharp surplus of large particles is visible near the evaporation front at all times, in which the particles are not mobile, indicating a jammed solid-like phase (Fig. 4**a-c**). As a measure for this surplus, we compute the volume fraction ratio (R_L) via:

$$R_L(x,t) = \frac{\phi_L(x,t)}{\phi_L(x,t) + \phi_S(x,t)} \quad (1)$$

in which $\phi_L(x,t)$ and $\phi_S(x,t)$ are the local volume fractions at time t (shown in Fig. 4**d-i**). Plotting R_L confirms the strong influence of the starting concentration on the jammed layer: while $\phi_{S,0}$= 0.025 features only a slight local excess of large particles, which partly disappears over time (Fig. 4**j**), for higher $\phi_{S,0}$ a quite pronounced excess of large particles is observed (Fig. 4**k,l**). Also the thickness of this layer increases with increasing initial ϕ_S. After ~20 h of evaporation, the jammed zone of $\phi_{S,0}$= 0.025 is highly reduced and not clearly visible any more in the confocal micrographs (Fig. 4**a**). By contrast, for $\phi_{S,0}$= 0.050 a jammed layer with sharp excess of large particles is visible (Fig. 4**b**). This band is even thicker for $\phi_{S,0}$= 0.10 (Fig. 4**c**). Most likely, a larger initial ϕ_S leads to a faster build-up of steep particle concentration gradients near the evaporation front, and consequently a larger region where ϕ exceeds the critical jamming fraction.

Behind the jammed region, diffusiophoresis-driven stratification is visible in all samples, which appears after ~6.5 h when the evaporation rate decreases (Fig. 4**d-i** and Fig. S4). For $\phi_{S,0}$= 0.025, the large particles are partly expelled from the area directly behind the jammed front (Fig. 4**d,g,j**). For $\phi_{S,0}$= 0.050, this band is even clearer, and additionally a local minimum in ϕ_L emerges after ~13 h (Fig. 4**e,h,k**). The increased initial volume fraction of the small particles gives rise to a stronger concentration gradient, resulting in a stronger expulsion of the large particles. Interestingly, further increasing $\phi_{S,0}$ to 0.10 does not further enhance the intensity of the third region, even though the small particles accumulate more strongly behind the jamming layer (Fig. 4 **f,i,l**). Most probably, the high total volume fraction in this sample leads to slower diffusion due to particle interactions, thus reducing the diffusiophoretic drift speed. Since the evaporation front propagates at unaltered rate, the large particles that are too slowly expelled will be included in the jamming front. Consequently, this sample features the most pronounced excess of large particles in the jamming layer (Fig. 4**c**), while the optimum for diffusiophoretic demixing is at $\phi_{S,0}$= 0.05. See Movies S2, S3 and Fig. S6, S7 for the full time series of all the collected images and concentration profiles corresponding to $\phi_{S,0}$= 0.025 and $\phi_{S,0}$= 0.10, respectively.

3.4. Theoretical prediction of the developing concentration profiles

To gain a deeper understanding of the mechanisms underlying stratification, we proceed to establish theoretical predictions of our experimentally measured volume fractions. Matching the spatiotemporally resolved ϕ profiles allows us to pinpoint the key phenomena governing stratification. In the Supporting Information, sections **2.1–2.5**, we provide comprehensive details of our theoretical model, and sequentially incorporate different elements

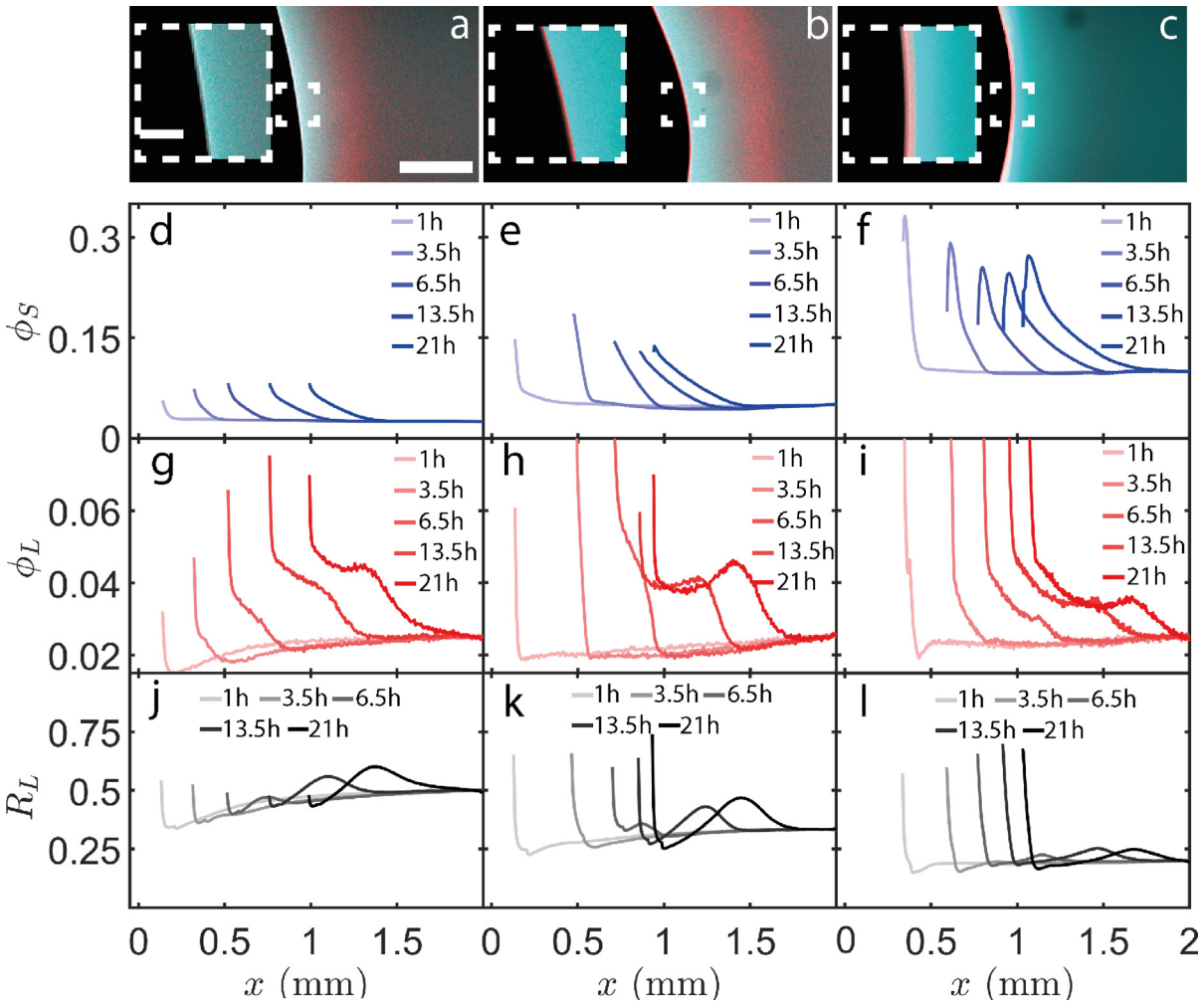

Fig. 4. Superimposed confocal micrographs of a drying binary dispersion after 20 h of evaporation for samples $\phi_{S,0}$ = 0.025(a), 0.050 (b) and 0.10 (c). The insets show a zoom of the evaporation interface. The scale bar in (a) represents 0.5 mm, and that in the inset 0.25 mm. They apply to all images. d-f) ϕ_S and (g-i) ϕ_L profiles after 1 h (lightest shade) 3.5 h, 6.5 h, 13.5 h and 21 h (darkest shade) from the start of drying. The columns represent $\phi_{S,0}$ = 0.025, 0.050 and 0.10, respectively. j-l) Excess of large or small particles computed from (a-f) using **Eq. 1**. Increasing $\phi_{S,0}$ increases the excess of large particles in the jammed layer, while the excess of large particles in the third region shows an optimum for $\phi S,0$ of 0.05.

to highlight the resulting effects (**Fig. 5**). We use the average time-resolved evaporation rate of the three samples to optimally mimic the experimental conditions (**Fig. S4d**). We start our theoretical framework from the pioneering model for colloidal stratification proposed by Zhou et al., which is founded on a second virial hard-sphere approximation (**Fig. 5a-b**) [17]. While this approach captures the asymmetric cross interactions to some extent, it is clear that the second virial approximation becomes inaccurate especially in the later stages of drying, when the volume fractions at the front become very high. We therefore modify the theory by adopting a more accurate expression for the free energy of the mixture, based on the equation of state proposed by Mansoori et al. for binary mixtures of hard spheres [47], which has been shown to be accurate up to volume fractions approaching close packing. The profiles predicted using this more accurate thermodynamic expression show a similar stratification as for the second virial approximation, but the higher-order interactions lead to a lower total volume fraction at the drying front (**Fig. 54c-d**). As discussed above, our experimental results strongly suggest the formation of a jammed region of particles immediately behind the drying front, where particle motion is arrested. To account for this jammed region, we assume that the particle diffusion coefficients gradually decrease with increasing volume fraction, until they are completely immobilized at a critical volume fraction. We find a very good match between experiments and theory when we use a smooth S-shaped decline of D for both species between $0.05 < \phi_S + \phi_L < 0.30$ (**Fig. 5e-f, Fig. S8**). These volume fractions are lower than those where hard spheres typically arrest, which may be due to a long-ranged electrostatic repulsion between the charged particles, which has been shown to significantly reduce diffusion already at $\phi \approx 0.3$[42]. Finally, we have also considered the effects of solvent backflow and electrostatic repulsion on our model predictions, but found these to be relatively small (**Fig. 5g-j**).

Combining all of the above described components leads to excellent agreement between the main experimental and theoretical trends; see **Fig. 6a,c** for comparisons of the final ϕ profiles. First, we find a clear excess of large particles near the evaporation front, where local accumulation leads to a jammed layer (**Fig. 6c**). Second, the extent of diffusiophoresis-driven demixing reaches an optimum at intermediate $\phi_{S,0}$: only in the $\phi_{S,0}$= 0.050 sample we observe a distinct dip in ϕ_L at $x \approx 1.0$ mm (**Fig. 6c**). Thirdly, the spatial extent of the diffusiophoretic stratification increases for higher $\phi_{S,0}$, which is visible in the position of the secondary maximum of the ϕ_L (**Fig. 6a,c**). To quantitatively examine this effect over time, we determine the spatial extent of diffusiophoretic demixing (Δ) as the distance between the secondary maximum of R_L (**Fig. 4g-i**,

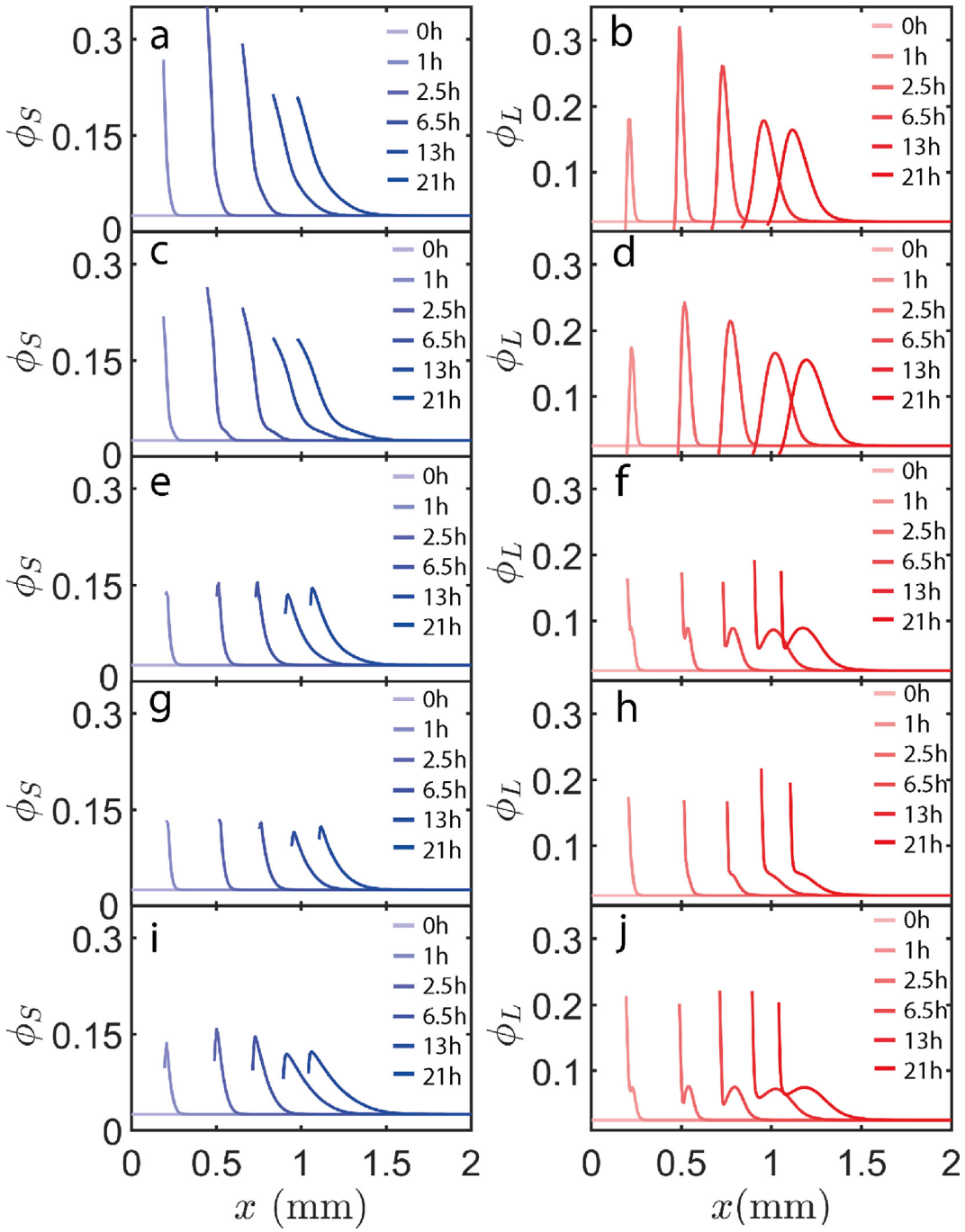

Fig. 5. Theoretical predictions of ϕ_S (first column) and ϕ_L (second column) after ~ 0 h (lightest shade), 1 h, 2.5 h, 6.5 h, 13 h and 21 h (darkest shade) of drying for $\phi_{S,0}$ = 0.025, based on only second order virial coefficients (a,b); higher-order particle–particle interactions (c,d); higher-order particle–particle interactions and slowing down of particle dynamics ($0.05 < \phi < 0.30$) (e,f); higher-order particle–particle interactions, slowing down of particle dynamics ($0.05 < \phi < 0.30$) and solvent backflow (g,h); and higher-order particle–particle interactions, a larger effective radius (50 nm), solvent backflow and slowing down of particle dynamics ($0.05 < \phi < 0.30$) (i,j); All the ingredients are essential to predict the volume fractions in a decent way.

Fig. S9) and the position of the evaporation front for both experimental (Fig. 6**b**) and theoretical (Fig. 6**d**) data. At the beginning, these extremum values are not yet present, but after several hours of drying they arise clearly. (Fig. 6**b,d**). In both experiments and theoretical predictions, we find an approximately linear relationship between Δ^2 and the evaporation time for all samples, underlining that particle segregation in these regions is driven by the collective diffusion of the small particles. Furthermore Δ rises faster for higher initial volume fractions. The thermodynamic driving force for diffusiophoresis, namely the osmotic pressure gradient of the small species, can reach higher values for higher initial ϕ_S. The associated steep ϕ_S profile builds up over length scales of >0.5 mm at $t = 21$ h (Fig. 4**c**), due to enhanced collective diffusion. Note that while the $\phi_{S,0}$ = 0.10 sample displays a large length scale of demixing, the associated amount is smaller compared to the other samples, as explained before. The high total volume fraction kinetically restrains the demixing process, thus limiting the extent of diffusiophoretic segregation.

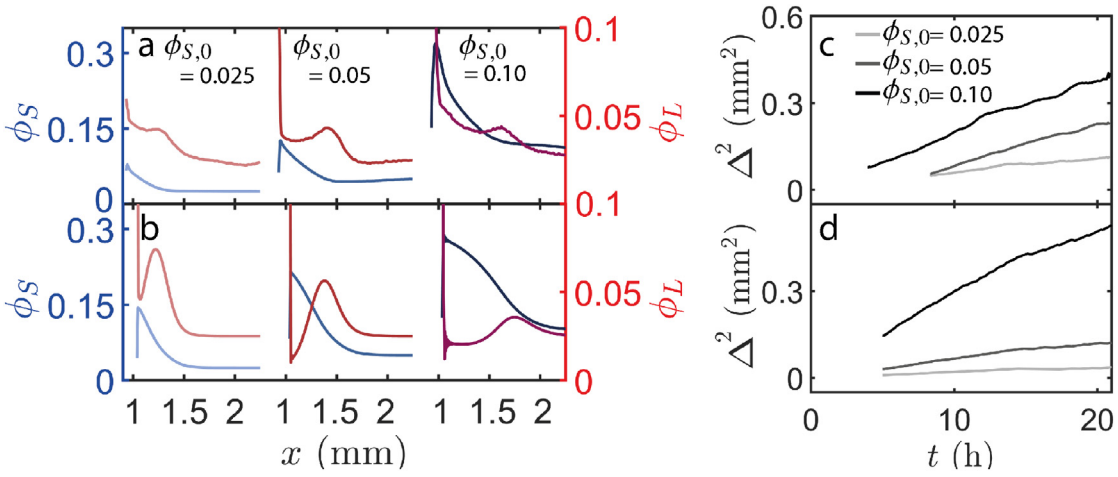

Fig. 6. Experimental (a) and theoretical (b) profiles of ϕ_S (blue) and ϕ_L (red) after ~21 h of drying. The derived diffusiophoretic distance Δ^2 over time for the experimental data (c) and theoretical data (d). Similar trends as the experimental data are visible in a jamming front with excess of large particles, an optimum in the amount of diffusiophoretic demixing for $\phi_{S,0}$= 0.050, a linear increase in diffusiophoretic demixing and time and a faster increase in Δ^2 for higher $\phi_{S,0}$.

Although our theoretical model reconstructs the experimental trends well, we observe mismatches in the exact volume fractions and Δ. These discrepancies are partially technical in origin, because the conversion of fluorescence intensities to volume fractions deviates from the assumed linear trend at high volume fractions (**Fig. 3c**). The experimentally determined volume fractions in the jamming front are thus underestimated. Moreover, our model does not include wall effects and spatial heterogeneities in the y, z directions, which could occur due to e.g. small density mismatches between the colloids and medium, yet only incorporates (moving) boundary conditions along x. Furthermore, effects arising from Marangoni flows, due to gradients in (trace amounts of) surfactants [9] and/or particle adsorption at the formamide–air interface could play a minor role in the final stratification pattern (**Fig. S10, SI 1.5**), yet these phenomena are neglected in our theoretical model. Finally, the practical reality is inevitably more complex than the theoretical representation, featuring small contributions from particle polydispersity, spatiotemporal gradients in salt and surfactant concentration, complex ϕ-dependent variations in the particle diffusion coefficients, etc. Nevertheless, our model captures and underlines the essence of particle–particle interactions, solvent backflow, and variable particle mobility to describe the evolving stratification in binary suspensions.

4. Conclusions

Auto-stratification in drying multi-component colloidal dispersions occurs via the build-up of concentration gradients and resultant changes in dynamics and interactions. While a substantial body of work has been devoted to elucidating this intricate process, experimental research to date has been focused on the end state [7,11,33,24,34,27]. Yet, untangling all layers of complexity requires direct spatial and temporal access to the colloidal concentrations.

In this work, we image and quantify the evolving volume fraction profiles in drying binary colloidal dispersions. By monitoring the profiles of both types of particles in time and comparing to numerical simulations, we find that the stratification process proceeds in a much more complex manner than commonly assumed. In particular, we show that the interplay between particle jamming near the moving drying front and colloidal diffusiophoresis in the region underneath gives rise to a structure consisting of three different layers. Both jamming and diffusiophoresis are rooted in the intrinsically out-of-equilibrium nature of drying, yet jamming is purely kinetic in origin, while diffusiophoresis is shaped by asymmetric interactions between the two particle species. The first layer initiates at the rapidly receding evaporation front, which sweeps up primarily the slower-diffusing large particles. Consequently, a critical volume fraction is reached locally, causing dynamic arrest of the particles. Behind this thin jammed layer, more gradual yet mobile concentration gradients emerge over time. Because both thermodynamic and hydrodynamic forces are size-dependent, the larger particles are effectively pushed deeper into the capillary, i.e. they move away from the second region by diffusiophoresis away from the second region. The resultant fractionation grows over progressively larger distances.

To elucidate the governing mechanisms in more detail, we have mapped the spatiotemporally heterogeneous concentration profiles onto theoretical predictions from a three-pillar numerical model. The foundations of our model are inspired by previous work, notably asymmetric particle interactions[17], solvent backflow[15,14], and particle jamming beyond a critical volume fraction. We show that merging all of these ingredients is essential to describe the intricate, dynamic interplays in our three-component system. In addition, inter-particle interactions beyond the second-virial approach and concentration-dependent diffusion coefficients appear indispensable extensions to the existing theories.

Both experimentally and numerically, we confirm that altering the initial volume fraction of the small particles is a powerful tuning knob for the extent of the two stratification modes, and hence the final layered structure. Specifically, the thickness of the jammed interfacial region increases monotonically with increasing ϕ_S. The widths and intensities of the diffusiophoretically size-separated layers display a less clear-cut trend: at low $\phi_{S,0}$, the concentration gradients are shallower and hence the diffusiophoretic force remains smaller, while at high $\phi_{S,0}$, the colloidal dynamics are slower and thus the migration of particles is restricted.

Our combined experimental and numerical approach provides new handles to e.g. study the effects of evaporation rate, particle sizes, volume fraction of the large species, particle interaction potential, medium viscosity, etc. For future work we envision expansion by imparting functional physical [48] or chemical [24] properties to the particles, so that the established layers in e.g. coatings gain different desired macroscopic properties.

Declaration of Competing Interest

The authors declare that they have no known competing financial interests or personal relationships that could have appeared to influence the work reported in this paper.

Acknowledgements

Funding: This work is part of the Advanced Research Center for Chemical Building Blocks, ARC CBBC, which is co-founded and co-financed by the Dutch Research Council (NWO) and the Netherlands Ministry of Economic Affairs and Climate Policy.

Author Contributions: E.H., H.M.v.d.K., T.E.K., J.S. and J.v.d.G. conceived the study. E.H., M.K. and T.E.K., synthesized and characterized the fluorescent colloids. E.H. performed the experiments and data analysis. E.H. and J.v.d.G. performed the simulations. All authors discussed the data and their interpretation and co-wrote the manuscript.

Competing Interests: The authors declare that they have no competing interests.

Data and materials availability: All data needed to evaluate the conclusions in this paper are present in the paper or the Supplementary Materials. Additional data may be requested from the authors.

Appendix A. Supplementary material

Supplementary data associated with this article can be found, in the online version, at https://doi.org/10.1016/j.jcis.2022.10.103.

References

[1] J. Sui, Transport dynamics of charged colloidal particles during directional drying of suspensions in a confined microchannel, Phys. Rev. E 99 (6) (2019) 062606.
[2] O. Cusola, S. Kivistö, S. Vierros, P. Batys, M. Ago, B.L. Tardy, L.G. Greca, M.B. Roncero, M. Sammalkorpi, O.J. Rojas, Particulate coatings via evaporation-induced self-assembly of polydisperse colloidal lignin on solid interfaces, Langmuir 34 (20) (2018) 5759–5771.
[3] H.M. van der Kooij, J. Sprakel, Watching paint dry; more exciting than it seems, Soft Matter 11 (32) (2015) 6353–6359.
[4] R. Antonelli, R. Fokkink, N. Tomozeiu, J. Sprakel, T. Kodger, High-speed laser speckle imaging to unravel picoliter drop-on-demand to substrate interaction, Rev. Sci. Instrum. 92 (8) (2021) 083906.
[5] W. Liu, J. Midya, M. Kappl, H.-J. Butt, A. Nikoubashman, Segregation in drying binary colloidal droplets, ACS nano 13 (5) (2019) 4972–4979.
[6] J. Keddie, A.F. Routh, Fundamentals of latex film formation: processes and properties, Springer Science & Business Media, 2010.
[7] M. Schulz, J. Keddie, A critical and quantitative review of the stratification of particles during the drying of colloidal films, Soft matter 14 (30) (2018) 6181–6197.
[8] J. Sui, Stratification in the dynamics of sedimenting colloidal platelet–sphere mixtures, Soft Matter 15 (23) (2019) 4714–4722.
[9] A.F. Routh, Drying of thin colloidal films, Rep. Prog. Phys. 76 (4) (2013) 046603.
[10] Y. Li, F. Liu, S. Chen, A. Tsyrenova, K. Miller, E. Olson, R. Mort, D. Palm, C. Xiang, X. Yong, et al., Self-stratification of amphiphilic janus particles at coating surfaces, Materials Horizons 7 (8) (2020) 2047–2055.
[11] A. Fortini, I. Martín-Fabiani, J.L. De La Haye, P.-Y. Dugas, M. Lansalot, F. D'agosto, E. Bourgeat-Lami, J.L. Keddie, R.P. Sear, Dynamic stratification in drying films of colloidal mixtures, Physical review letters 116 (11) (2016) 118301.
[12] R. Trueman, E. Lago Domingues, S. Emmett, M. Murray, and A. Routh, "Auto-stratification in drying colloidal dispersions: A diffusive model," Journal of Colloid and Interface Science, vol. 377, pp. 207–212, Jul 2012.
[13] J.H. Jeong, Y.K. Lee, K.H. Ahn, Stratification mechanism in the bidisperse colloidal film drying process: Evolution and decomposition of normal stress correlated with microstructure, Langmuir 37 (46) (2021) 13712–13728.
[14] R.P. Sear, P.B. Warren, Diffusiophoresis in nonadsorbing polymer solutions: The asakura-oosawa model and stratification in drying films, Phys. Rev. E 96 (6) (2017) 062602.
[15] R.P. Sear, Stratification of mixtures in evaporating liquid films occurs only for a range of volume fractions of the smaller component, The Journal of chemical physics 148 (13) (2018) 134909.
[16] C.R. Rees-Zimmerman, A.F. Routh, Stratification in drying films: a diffusion–diffusiophoresis model, J. Fluid Mech. 928 (2021).
[17] J. Zhou, Y. Jiang, M. Doi, Cross interaction drives stratification in drying film of binary colloidal mixtures, Phys. Rev. Lett. 118 (10) (2017) 108002.
[18] D. Makepeace, A. Fortini, A. Markov, P. Locatelli, C. Lindsay, S. Moorhouse, R. Lind, R. Sear, J. Keddie, Stratification in binary colloidal polymer films: Experiment and simulations, Soft Matter 13 (39) (2017) 6969–6980.
[19] A. Fortini, R.P. Sear, Stratification and size segregation of ternary and polydisperse colloidal suspensions during drying, Langmuir 33 (19) (2017) 4796–4805.
[20] M.P. Howard, A. Nikoubashman, Stratification of polymer mixtures in drying droplets: Hydrodynamics and diffusion, J. Chem. Phys. 153 (5) (2020) 054901.
[21] A. Statt, M.P. Howard, A.Z. Panagiotopoulos, Influence of hydrodynamic interactions on stratification in drying mixtures, The Journal of chemical physics 149 (2) (2018) 024902.
[22] Y. Tang, G.S. Grest, S. Cheng, Control of stratification in drying particle suspensions via temperature gradients, Langmuir 35 (12) (2019) 4296–4304.
[23] X. Liu, W. Liu, A.J. Carr, D.S. Vazquez, D. Nykypanchuk, P.W. Majewski, A.F. Routh, S.R. Bhatia, Stratification during evaporative assembly of multicomponent nanoparticle films, Journal of colloid and interface science 515 (2018) 70–77.
[24] Y. Dong, M. Argaiz, B. He, R. Tomovska, T. Sun, I. Martín-Fabiani, Zinc oxide superstructures in colloidal polymer nanocomposite films: Enhanced antibacterial activity through slow drying, ACS Applied Polymer Materials 2 (2) (2020) 626–635.
[25] Y. Dong, N. Busatto, P.J. Roth, I. Martin-Fabiani, Colloidal assembly of polydisperse particle blends during drying, Soft Matter 16 (36) (2020) 8453–8461.
[26] A.K. Atmuri, S.R. Bhatia, A.F. Routh, Autostratification in drying colloidal dispersions: Effect of particle interactions, Langmuir 28 (5) (2012) 2652–2658.
[27] M. Schulz, C. Crean, R. Brinkhuis, R. Sear, J. Keddie, Determination of parameters for self-stratification in bimodal colloidal coatings using raman depth profiling, Prog. Org. Coat. 157 (2021) 106272.
[28] A. Samanta, R. Bordes, On the effect of particle surface chemistry in film stratification and morphology regulation, Soft Matter 16 (27) (2020) 6371–6378.
[29] M. Schulz, R.W. Smith, R.P. Sear, R. Brinkhuis, J.L. Keddie, Diffusiophoresis-driven stratification of polymers in colloidal films, ACS Macro Letters 9 (9) (2020) 1286–1291.
[30] A.J. Carr, W. Liu, K.G. Yager, A.F. Routh, S.R. Bhatia, Evidence of stratification in binary colloidal films from microbeam x-ray scattering: Toward optimizing the evaporative assembly processes for coatings, ACS Applied Nano Materials 1 (8) (2018) 4211–4217.
[31] W. Liu, A.J. Carr, K.G. Yager, A.F. Routh, S.R. Bhatia, Sandwich layering in binary nanoparticle films and effect of size ratio on stratification behavior, Journal of colloid and interface science 538 (2019) 209–217.
[32] I. Martín-Fabiani, A. Fortini, J. Lesage de la Haye, M.L. Koh, S.E. Taylor, E. Bourgeat-Lami, M. Lansalot, F. D'agosto, R.P. Sear, J.L. Keddie, ph-switchable stratification of colloidal coatings: surfaces "on demand, ACS applied materials & interfaces 8 (50) (2016) 34755–34761.
[33] I. Nikiforow, J. Adams, A.M. König, A. Langhoff, K. Pohl, A. Turshatov, D. Johannsmann, Self-stratification during film formation from latex blends driven by differences in collective diffusivity, Langmuir 26 (16) (2010) 13162–13167.
[34] M. Schulz, R. Brinkhuis, C. Crean, R. Sear, J. Keddie, Suppression of self-stratification in colloidal mixtures with high péclet numbers, Soft Matter 18 (13) (2022) 2512–2516.
[35] H. Luo, C.M. Cardinal, L. Scriven, L.F. Francis, Ceramic nanoparticle/monodisperse latex coatings, Langmuir 24 (10) (2008) 5552–5561.
[36] P. Ekanayake, P. McDonald, J. Keddie, An experimental test of the scaling prediction for the spatial distribution of water during the drying of colloidal films, The European Physical Journal Special Topics 166 (1) (2009) 21–27.
[37] W. Liu, J. Shen, S.R. Bhatia, An in-situ saxs approach to probe stratification during drying of inorganic nanoparticle films, Inorg. Chim. Acta 517 (2021) 120213.
[38] K. Thitiporn and J.F. Gilchrist, "Chemical vs. mechanical microstructure evolution in drying colloid and polymer coatings," Scientific Reports (Nature Publisher Group), vol. 10, no. 1, 2020.
[39] T.E. Kodger, R.E. Guerra, J. Sprakel, Precise colloids with tunable interactions for confocal microscopy, Scientific reports 5 (2015) 14635.
[40] S. Shin, E. Um, B. Sabass, J.T. Ault, M. Rahimi, P.B. Warren, H.A. Stone, Size-dependent control of colloid transport via solute gradients in dead-end channels, Proc. Nat. Acad. Sci. 113 (2) (2016) 257–261.
[41] M. Egen and R. Zentel, "Surfactant-free emulsion polymerization of various methacrylates: towards monodisperse colloids for polymer opals," Macromolecular chemistry and physics, vol. 205, no. 11, pp. 1479–1488, 2004.
[42] A. Van Blaaderen, J. Peetermans, G. Maret, J. Dhont, Long-time self-diffusion of spherical colloidal particles measured with fluorescence recovery after photobleaching, The Journal of chemical physics 96 (6) (1992) 4591–4603.
[43] M. Yu, C. Le Floch-Fouéré, L. Pauchard, F. Boissel, N. Fu, X.D. Chen, A. Saint-Jalmes, R. Jeantet, L. Lanotte, Skin layer stratification in drying droplets of dairy colloids, Colloids Surf., A 620 (2021) 126560.

[44] J. Appell, G. Porte, E. Buhler, Self-diffusion and collective diffusion of charged colloids studied by dynamic light scattering, J. Phys. Chem. B 109 (27) (2005) 13186–13194.
[45] B. Sobac, S. Dehaeck, A. Bouchaudy, J.-B. Salmon, Collective diffusion coefficient of a charged colloidal dispersion: interferometric measurements in a drying drop, Soft matter 16 (35) (2020) 8213–8225.
[46] L. Goehring, J. Li, P.-C. Kiatkirakajorn, Drying paint: from micro-scale dynamics to mechanical instabilities, Philosophical Transactions of the Royal Society A: Mathematical, Physical and Engineering Sciences 375 (2093) (2017) 20160161.
[47] G. Mansoori, N.F. Carnahan, K. Starling, T. Leland Jr, Equilibrium thermodynamic properties of the mixture of hard spheres, J. Chem. Phys. 54 (4) (1971) 1523–1525.
[48] S. Hajeesaeh, S. Kariyo, N. Muensit, C. Daengngam, Self-stratifying particulate coating for robust superhydrophobic and latex-repellent surface, J. Environ. Treat. Tech. 8 (3) (2020) 1107–1111.